Polymer 49 (2008) 4285–4297

Contents lists available at ScienceDirect

Polymer

journal homepage: www.elsevier.com/locate/polymer

Quantification of organoclay dispersion and lamellar morphology in poly(propylene)–clay nanocomposites with small angle X-ray scattering

Nisha Preschilla [a], G. Sivalingam [a], A.S. Abdul Rasheed [b], Sandeep Tyagi [a], Amit Biswas [a], Jayesh R. Bellare [b,*]

[a] Polymer Research and Technology Centre, Reliance Industries Limited, V.N. Purav Marg, Chembur, Mumbai 400073, India
[b] Department of Chemical Engineering, Indian Institute of Technology Bombay, Powai, Mumbai 400071, India

ARTICLE INFO

Article history:
Received 24 January 2008
Received in revised form 15 July 2008
Accepted 20 July 2008
Available online 25 July 2008

Keywords:
Nanocomposites
Small angle X-ray scattering
Clay exfoliation

ABSTRACT

Intensity profiles of small angle X-ray scattering (SAXS) curves were analyzed to simultaneously gain quantitative information on nanoclay dispersion as well as lamellar ordering in polypropylene–clay nanocomposites. Different types of PP nanocomposites prepared with PP homopolymer (HPP), random propylene–ethylene copolymer (RCP) and a high impact polypropylene–ethylene propylene rubber (ICP) were analyzed. Various one-dimensional models for stacked structures were applied on Lorentz corrected SAXS spectra to derive long period, thicknesses of alternating high and low electron density layers and their distributions, and the number of stacks for both nanoclay and PP lamellae. We applied a mixed thickness distribution model comprising combined Gaussian and exponential for a simple stack of finite thickness, which was found to explain the experimental data better for both nanoclay tactoids and lamellar stacks, compared to simple Gaussian and exponential thickness distributions. Long period X and number of stacks N were derived as important parameters signifying changes in levels of nanoclay exfoliation in PP. Among the three types of polypropylenes studied, better nanoclay exfoliation was obtained for the high impact ICP grade compared to HPP and RCP. Complete exfoliation of nanoclay was achieved in ICP matrix, employing a masterbatch processing route. Moreover, role of nanoclay as a γ nucleating agent was evident from small and wide angle X-ray analyses, and was seen strongly in RCP. Changes in lamellar structure of PP as a result of nanoclay incorporation, double population consisting of both α and γ polytypes in the nanocomposites from that of a primarily α population in neat polymer matrices, were also analyzed in detail with the mixed thickness distribution model, thereby demonstrating its usefulness.

1. Introduction

Development of polymer-layered silicate nanocomposites (PLSNs) has been an area of high research interest in the past few years, as a result of manifold property enhancements achievable in these materials [1–5]. This improved performance, remarkably augmented from that of the inherent properties of virgin polymer, is seen as increased modulus, tensile strength and heat resistance, higher barrier to moisture and gas, and superior flame retardance [6–10]. Since the successful demonstration of full exfoliation and homogeneous dispersion of nanoclay in nylon-6 with exceptional properties attained at low loadings by Toyota researchers [7,11], large efforts have gone into the development of similar nanocomposites in other polymer matrices. A wide range of polymers such as vinyl polymers, polycondensates, polyolefins and specialty polymers have been explored along with natural clays or synthetic layered silicates for the development of PLSNs [3]. Large efforts have also gone into organic modification of nanoclays by ion-exchange reactions with cationic surfactants like alkylammonium or alkyl phosphonium cations in order to convert its hydrophilic surface into an organophilic one, and thus make them compatible with most polymers [12,13]. Furthermore, different processing routes such as *in situ* polymerization, polymer intercalation from solution, melt intercalation and ultrasonication have been explored in-depth to effectively exfoliate and uniformly disperse clay platelets in polymer matrices [14–18]. Basically three different levels of exfoliation of nanoclay are seen in polymer matrices: a non-exfoliated system where nanoclay particles are seen to remain as a stacked structure consisting of a very large number of platelets with interlayer spacing equivalent to that of neat nanoclay, an intercalated case wherein an expansion of clay platelets is observed resultant of polymer chain penetration into the interlayer

* Corresponding author. Tel.: +91 22 25767207; fax: +91 22 25726895.
E-mail address: jb@iitb.ac.in (J.R. Bellare).

0032-3861/$ – see front matter © 2008 Elsevier Ltd. All rights reserved.
doi:10.1016/j.polymer.2008.07.030

spacing, and partly to complete exfoliation with individual silicate layers dispersed in the matrix [3]. Engineering performance of PLSNs is observed to be maximal when complete exfoliation of nanoclays into single platelets homogeneously dispersed throughout the polymer is achieved.

Polypropylene (PP) is one of the widely used polymers due to its attractive combination of good processability, physical properties and chemical resistance, and therefore finds high-volume applications in many sectors such as automotive, packaging and appliances [19]. PP based PLSN is of high commercial significance; incorporation of nanoclay into PP is expected to further improve stiffness, strength and barrier performance. However, exfoliating nanoclay in polypropylene has been challenging, as a result of surface polarity mismatch between PP and clay even after the nanoclays are organically modified. The most commonly used approach to further aid compatibilization and dispersion of organoclays in PP is by melt compounding with maleic anhydride grafted PP (MA-PP) [20–22]. This method is found to be effective to a great extent, but leads to loss of properties, as a result of high concentrations of MA-PP required for complete exfoliation of nanoclays. *In situ* polymerization methods employing Ziegler–Natta catalysts and metallocene catalysts are reported to result in better nanoclay exfoliation in PP, though highly uniform dispersion of clay platelets was not achieved [23]. Use of supercritical fluids for pre-exfoliation of nanoclays [24] and *in situ* ultrasonication [17] during melt compounding are other effective approaches used in successful exfoliation of nanoclays in PP.

Objective of this work is twofold: develop PP based PLSNs employing different PP matrices and novel organoclays, and concurrently develop the much needed quantitative methods to evaluate nanoclay exfoliation. Need for such analytical tools is evident from the fact that parallel to the extensive focus on the material and processing aspects in developing PLSNs, investigations on characterization methods that conclusively explain various hierarchical organic and inorganic structures in PLSNs in understanding their properties have also been widely reported. Structure, morphology and degree of exfoliation of nanoclays are generally studied by a combination of transmission electron microscopy (TEM) and X-ray scattering methods [3,12,25–30]. Applications of NMR [31,32] and FTIR spectroscopies [33,34] have also been reported to understand exfoliation and orientation effects. With TEM, qualitative visual evaluation of nanoclay dispersion is generally carried out. Tedious quantifications based on image analysis on a large set of images are required to arrive at statistically valid estimations representative of bulk of the material. Monitoring intensity and interlayer spacing corresponding to basal reflections from nanoclay layers in X-ray scattering based techniques is another widely adopted methodology. Depending on the level of exfoliation, the basal peak shifts to lower angles in the case of intercalation, whereas peak intensity decreases when partly exfoliated to eventual disappearance as the clay layers exfoliate completely. In the case of PLSNs based on semicrystalline polymers such as PP, it becomes equally important to understand the nature of dispersity of crystalline lamellae and changes in crystallographic organizations, in addition to assessing nanoclay dispersion. In such cases, a comprehensive study involving a combination of small angle and wide angle X-ray scattering to resolve hierarchical structural organizations of nanoclay and polymer is a rational approach.

Analysis of SAXS intensity profiles of ordered lamellar stacks with various one-dimensional models is well studied, widely used techniques being correlation functions and interface distribution functions [35–39], Hosemann's general models [40,41] and Ruland's stacking models and lattice models [42]. All these approaches can be related to the lamellar structure only with reference to a morphological model, a basic model which assumes that the lateral width of lamellae is much larger than the long period normal to the lamellae and the electron density varies with a rectangular profile for alternating crystalline and amorphous layers. Correlation function $\gamma(r)$ is derived from the experimental scattered intensities as an inverse cosine Fourier transform and is also a measure of the self-correlation profile of electron density in lamellar stacks at distance r. The interface distribution function $g(r)$ can be estimated as second derivative of the correlation function, and also represents the probability of finding two interfaces within r. These methods have been applied extensively to the study of lamellar stacks in numerous semicrystalline polymers such as poly(ethylene terephthalate) [36,43], poly(ether ether ketone) [39], poly(oxymethylene) [44], polypropylene [45–47] and linear polyethylene [37]. In the case of highly dispersed lamellae resulting in broad diffraction peaks, a more appropriate approach is Hosemann's general model, wherein theoretical scattering profiles are calculated as the sum of separate contributions from Babinet and crystalline components. The crystalline component shows an inverse dependence on number of stacks becoming prominent as the stack dimension becomes smaller and leads to peak broadening. This approach was applied to study broad diffraction patterns from low density polyethylene [41], high density polyethylene [48] polypropylene [38,49,50] and poly(butene) [51], and models consisting of statistically uniform stacks with a finite size – known as the finite lamellar stack model – as well as a variable stack model which also takes into account that a spatial variation in local crystallinity was seen to agree better with experimental intensity profiles than a simple stack of infinite width. Lattice model is based on two distributions; one that of a lattice with varying lattice parameters in space, with its lattice points defined as the centre of each stacks. The other distribution is for stack parameters that vary independent of lattice parameters. This model yields comparable results to that of Hosemann's stack model, though offers slightly better fit to the experimental curve [52]. From all the above approaches, various order parameters and their distributions corresponding to the lamellar stack such as the crystal thickness Y, the thickness of the amorphous region Z, long period X which is the sum of Y and Z, and number of stacks N can be estimated. Volume fractions of local crystalline and amorphous phases are estimated as the ratio of crystalline or amorphous layer thickness to long period. Assignment of these average dimensions Y and Z in correlation functions and interface distribution functions is arbitrary, and is usually based on inferences from volume crystallinity measurements. However, in Hosemann's model, these values are parameters distinctly defined to generate the theoretical intensity profile and hence can be considered valid. Another relevant parameter that can be estimated from $\gamma(r)$ is the thickness t of a phase boundary between the crystalline and adjacent amorphous regions, which can be used to define an actual two-phase structure for electron density profile which is more realistic than the ideal two-phase structure, nevertheless it is often not employed since the transition zones do not influence the values of X, Y, Z and other parameters in a substantial manner.

An extended application of Hosemann's model to SAXS patterns corresponding to clay layers, consisting of alternating high electron density silicate layers with low electron density regions interposed, taking into consideration the geometrical similarity in morphological distribution to that of lamellae. This approach was demonstrated by Causin et al. for the quantification of organoclay dispersion in polypropylene and poly(butene) [49–51,53,54]. Influence of additives and processing conditions on extent of nanoclay dispersion was explained with quantitative data such as the number of clay layers, interlayer spacing and its distributions. Model parameters were verified with extensive TEM and wide angle X-ray studies. This approach highlighted the definite advantage of SAXS methods, as they are representative of the bulk of the

sample, and does not have the ambiguities associated with sample preparation and two-dimensional projections as encountered in microscopic analysis of nanoclays.

In this work, evaluation of nanoclay dispersion depending on various processing routes in different PP homopolymer, random copolymer and high impact PP–ethylene propylene rubber (EPR) compositions was performed with emphasis on application of Hosemann's model to SAXS spectra. In addition to commonly employed Gaussian and exponential thickness distributions, a mixed thickness distribution was also explored for better explanation of SAXS intensity profiles. Detailed discussion on results obtained by all methods is given and correlation to mechanical properties is explained. Further, changes in crystallographic organizations of PP with nanoclay incorporation and role of nanoclay as a γ nucleating agent for PP are also discussed.

2. Experimental details

Three polypropylene grades manufactured by Reliance Industries Limited, India, were explored in this work for the development of PP nanocomposites. These included a homopolymer (HPP) with melt flow index (MFI) of 11 g/10 min, random copolymer (RCP) with MFI of 0.3 g/10 min and ethylene content of three weight fraction and finally, a high impact grade PP (ICP) which is reactor copolymerized ethylene–propylene rubber (EPR) dispersed in PP matrix, having an MFI of 1.5 g/min and rubber content of about 18%. Prime grade of a novel, organically modified nanoclay supplied by Crystal Nanoclay Private Limited, India, was used throughout this work. Basal spacing for the untreated clay was 1.2 nm. Maleated PP (MA-PP) was used as compatibilizer, and was used in an MA-PP:organoclay ratio of 1:1 in all the three nanocomposites. Nanocomposites with HPP RCP and ICP, i.e., HPP-NC, RCP-NC and ICP-NC1, respectively, with organoclay loading of 6wt% were prepared by direct compounding in a 30 mm Omega extruder with L/D of 40 and were tumble blended with virgin polypropylene granules for molding test specimen. For the high impact ICP grade, samples were also prepared by dilution of a masterbatch sample containing 30% organoclay, which is ICP-NC2, having final organoclay concentration of 6%.

Simultaneous small and wide angle X-ray scattering data were measured at room temperature from samples of 100 μm thickness in SAXSess (by Anton Paar, Austria) system with Ni filtered Cu K_α radiation source. Intensity profiles were obtained with a slit collimated compact Kratky camera and recorded with a two-dimensional imaging plate. Sample to detector distance was 265 mm and covers the scattering angle range $2\theta = 0.056°$–$40°$. Two-dimensional scattered data are linearly averaged to get intensity $I(q)$ vs. scattering vector q (nm^{-1}), where $q = 4\pi/\lambda(\sin\theta)$ and 2θ is the scattering divergence angle and λ is the Cu K_α X-ray wavelength. SAXS data in the range up to $q = 3.5\ nm^{-1}$ were first smoothed and then corrected by subtracting a constant background scattering value observed at angles intermediate of SAXS and WAXS. Desmearing of the slit smeared intensities was carried out using GIFT algorithm developed by Glatter [55] for lamellar structures. Finally, the one-dimensional SAXS profiles were obtained through Lorentz correction, with a multiplication of the desmeared intensity by a factor of $4\pi s^2$, where $s = q/2\pi$.

Bulk crystallinity and percentage components of α and γ polymorphs of PP were estimated from wide angle X-ray diffraction (WAXD) profiles after a liner background subtraction and deconvolution of the profile into crystalline and amorphous fractions, using a Gaussian lineshape for the peaks.

Transmission electron microscopic studies were performed on an FEI Tecnai G^2 TEM operated at 120 kV; 80 nm sections were prepared at −60 °C using a Leica UCT ultramicrotome, followed by vapor staining for 15 min with RuO_4.

3. Theoretical model for SAXS

Polypropylene-layered silicate nanocomposites have two ordered structures namely lamellae and organoclay and they are geometrically similar. In lamella, ordered structure is formed with the alternating crystalline and amorphous polymers, whereas for organoclay, the ordered structure is formed with inorganic materials like silicate and organic layers like modifiers or polymers. Length of the clay or lamellae is much longer than their thickness and therefore, length of the lamellae or organoclay can be regarded as infinite. This makes the problem to be solved in one dimension for both lamellae and organoclay stacks. Thickness profile of lamellae and organoclay is assumed as rectangular profile with high and low electron density layers as shown in Fig. 1 [41]. High electron density layer H represents the crystalline section/inorganic (silicates) of lamellae/organoclay. Low electron density layer L represents the amorphous section/modifier or polymer of lamellae/organoclay. Thickness of the ith high electron density crystalline layer of polymer/organoclay platelet is H_i, that of amorphous layer of polymer/interplanar spacing between clay layers in organoclay is L_i, the long period is $X_i = H_i + L_i$ and ρ_H and ρ_L are high and low electron densities, respectively. The local crystallinity within the lamellae can be estimated as $\Phi = H_i X_i$. In this study, a sharp transition at the interface between the layers is assumed and the thicknesses of high and low density layers are allowed to vary independent of each other. Hosemann's general model is applied to this stacked structure. For a stack consisting of N layers, the intensity profile is the sum of Babinet component $I_B(s)$ and crystalline components $I_c(s)$ and is written as [40]

$$I(s) = I_B(s) + I_c(s) \tag{1}$$

where

$$I_B(s) = \frac{(\rho_H - \rho_L)^2}{4\pi^2 s^2 X} \frac{|1 - F_H|^2\left(1 - |F_L|^2\right) + |1 - F_L|^2\left(1 - |F_H|^2\right)}{|1 - F_H F_L|^2} \tag{2}$$

and

$$I_c(s) = \frac{(\rho_H - \rho_L)^2}{2\pi^2 s^2 XN} Re\left\{\frac{F_L(1 - F_H)^2(1 - F_H F_L)^N}{(1 - F_H F_L)^2}\right\} \tag{3}$$

where F_H and F_L are Fourier transforms of the thickness distributions for H and L. One can note that Babinet component is not a function of number of layers in a stack and the crystalline component is inversely related to the number of layers. In the case of an infinite stack model ($N \to \infty$), the crystalline component

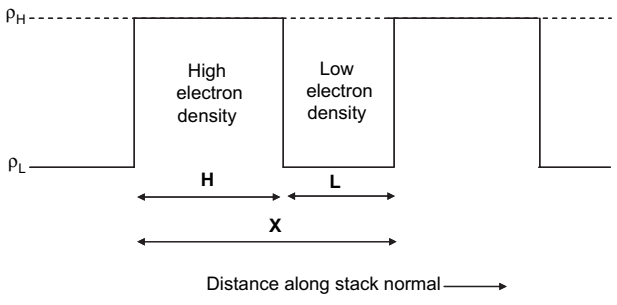

Fig. 1. One-dimensional electron density distribution for alternating layers in organoclay or semicrystalline lamellae [42]. High electron density layer H represents the crystalline layer for lamellae and silicate layer of organoclay. Low electron density layer L represents the amorphous section and modifier or polymer layer of lamellae and organoclay, respectively.

contribution, which is interference from the adjacent layers, diminishes and the total intensity thus becomes equivalent to the Babinet component. However, for a finite stack having higher dispersion of lamellar or nanoclay layers, $I_c(s)$ becomes significant and leads to broadening of the diffraction peaks. A further extension of the finite stack model is the variable stack model wherein a variation in local crystallinity between stacks is allowed.

Choosing an appropriate model from the simple infinite/finite stack or the variable stack that most represents the material, $I(s)$ can be easily computed if the thickness distribution functions for the layers H and L are appropriately chosen. Commonly, the thickness distributions are assumed to be either truly symmetrical (Gaussian distribution) or truly asymmetrical (exponential distribution). For symmetrical cases, thickness distribution for high electron density layer can be written as [56]

$$G(H) = \frac{1}{\sigma_H(2\pi)^{1/2}} \exp - \frac{(H-\overline{H})^2}{2\sigma_H^2} \tag{4}$$

where $\overline{H}$ and σ_H are the mean thickness and standard deviation, respectively. The corresponding Fourier transform is given as

$$F(H) = \exp\left(-2\pi^2 s^2 \sigma_H^2\right) \exp(-2\pi i s \overline{H}) \tag{5}$$

Similar expressions can be written for low electron density layer. The total standard deviation for single stack is $\sigma = \sigma_H^2 + \sigma_L^2$.

Contribution of individual Babinet and crystalline components to total SAXS intensity using Gaussian thickness distributions is given in Fig. 2. Effect of the crystalline component to total SAXS intensity as a destructive interference leading to peak broadening can be readily seen.

Similarly, for asymmetrical cases, the high electron density layer thickness distribution can be written as the exponential distribution [57]

$$E(H) = \begin{cases} 0 & \forall H < H_0 \\ \dfrac{1}{\sigma_H^*} \exp\left(\dfrac{-(H-H_0)}{\sigma_H^*}\right) & \forall H \geq H_0 \end{cases} \tag{6}$$

The Fourier transform of the exponential distribution, as given in Eq. (6), is given as

$$F_H = \frac{1}{1 + 2\pi i s \sigma_H^*} \exp(-2\pi i s H_0) \tag{7}$$

The mean of exponential distribution and Gaussian distribution can be related as $\overline{H} = H_0 + \sigma_H^*$.

Thickness distributions discussed above would be useful to explain the distributions which are truly symmetrical about the mean or truly asymmetrical. In practical cases, obtaining a perfect symmetrical or asymmetrical distribution is quite difficult even for the same polymer, under different additives/clay loadings and processing conditions employed. Hence, situations may warrant the shifting of the distributions from symmetrical to asymmetrical based on the problem. To ameliorate this problem, a hybrid model that is convolution of both symmetrical and asymmetrical distributions [41] which would serve as unified model for most of the practical cases is proposed. A Gaussian distribution was assumed for the symmetrical distribution and an exponential distribution for asymmetrical distribution. The hybrid distribution or the mixed thickness distribution is therefore represented by a convolution

$$M(H) = \int_{-\infty}^{\infty} G(p)E(H-p)\mathrm{d}p \tag{8}$$

where $G(H)$, is the Gaussian distribution and $E(H)$ is an exponential distribution, as given above. Since Fourier transform of the distribution is used to calculate the SAXS intensity, a product of the Fourier transforms for symmetrical and asymmetrical distributions becomes Fourier transform of the hybrid distribution. This generic Fourier transform reduces to a pure Gaussian or exponential distribution when σ_H or σ_H^*, respectively, tends to zero. Contribution of individual Babinet and crystalline components to total SAXS intensity for a mixed thickness distribution is given in Fig. 2. Theoretical SAXS patterns were modeled with all the three thickness distributions, i.e., Gaussian, exponential and mixed distributions mentioned above and structural parameters were thus derived.

Fig. 3 shows the effect of N on the total SAXS intensity for the mixed thickness distributions. Other model parameters were fixed at $X = 2.5$ nm, $H = 1.25$ nm and $L = 1.25$ nm, the standard deviations σ_H-exponential and σ_L-exponential are both 0.8 nm and σ_H-Gaussian and σ_L-Gaussian are 0.2 nm. It may be recalled that $I_B(s)$ is not dependent on N, and $I_c(s)$ has an inverse relationship with N, therefore $I(s) \to I_B(s)$ as $N \to \infty$. As N decreases, total SAXS intensity broadens due to the destructive intensity contribution from crystalline component [41]. For $N = 1$, the area under the Babinet

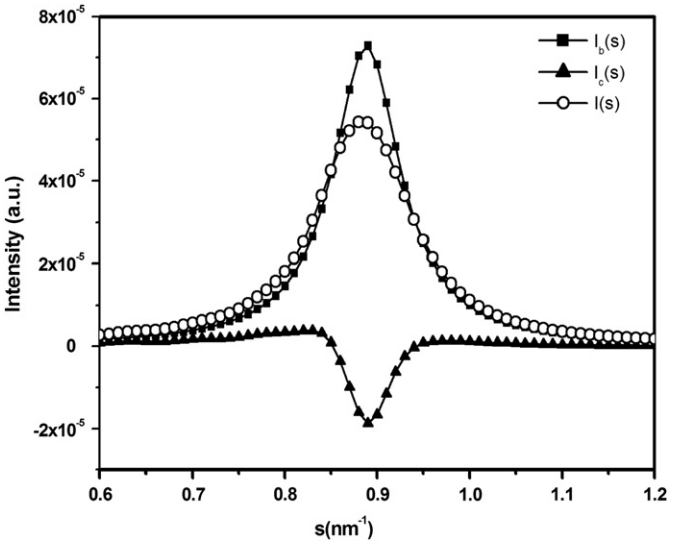

Fig. 2. Contribution of Babinet and crystalline components to total SAXS intensity.

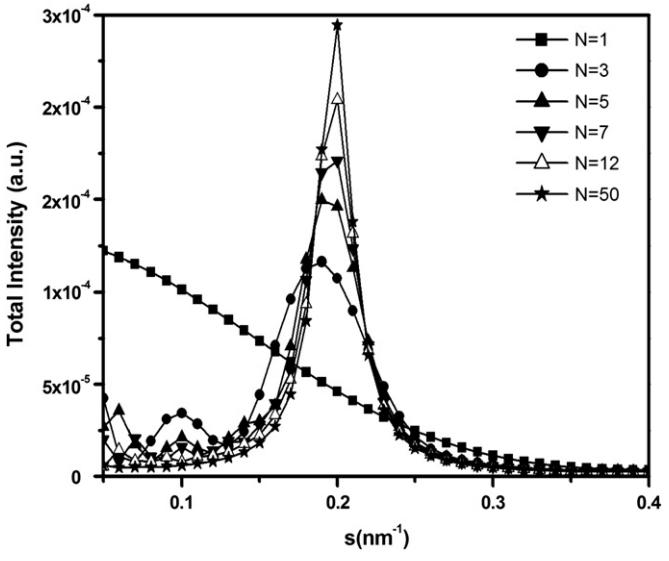

Fig. 3. Plot of N sensitivity showing the effect of number of layers on total SAXS response. Peak broadening effects with increasing dispersion of clay layers can be seen.

intensity component is same as that of area of crystalline intensity component, leading to absence of any SAXS peaks.

Effect of long period (X) on SAXS intensities is shown in Fig. 4(a) and (b), with $N = 7$, the standard deviations σ_H-exponential and σ_L–exponential used were 0.6 nm and σ_H-Gaussian and σ_L–Gaussian at 0.2 nm. Fig. 4(a) shows that the peak value of intensity varies linearly with X (R^2 is 1.0) for all three distributions. Fig. 4(b) further indicates that peak position is inversely proportional to X for Babinet, crystalline and total intensity. The proportionality constant is around 1.0 for all values of X, for all $I_c(s)$, $I_B(s)$ and the total intensity $I(s)$. When we convolute two functions, in the case of mixed distribution, actual X and Xq_{peak} are twice those of what is used in the distribution.

Fig. 5 shows the response of total intensity and the $I_c(s)$ and $I_B(s)$ components to Φ for the mixed thickness distribution. Other model parameters were $N = 7$, $X = 5$ nm, the standard deviations σ_H-exponential/σ_L–exponential = 0.6 nm and σ_H-Gaussian and σ_L–Gaussian were 0.2 nm. It can be seen that the SAXS response is symmetric and a maximum was exhibited at $\Phi = 0.5$ for $I(s)$, $I_c(s)$ and $I_B(s)$. Intensity values for all these cases reduce to zero at both $\Phi = 0$ and $\Phi = 1$, confirming the need for an electron density difference to obtain any SAXS response. It also confirms that the maximum SAXS response is obtained for a 50/50 phase fraction of high electron density/low electron density layer, which is the case when $H = L$.

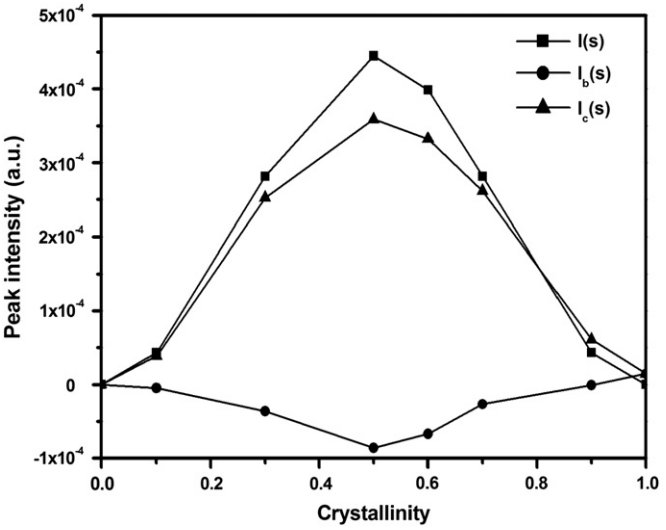

Fig. 5. Plots of Φ sensitivity of SAXS response for total intensity, $I_c(s)$ and $I_B(s)$ components to Φ for the mixed thickness distribution.

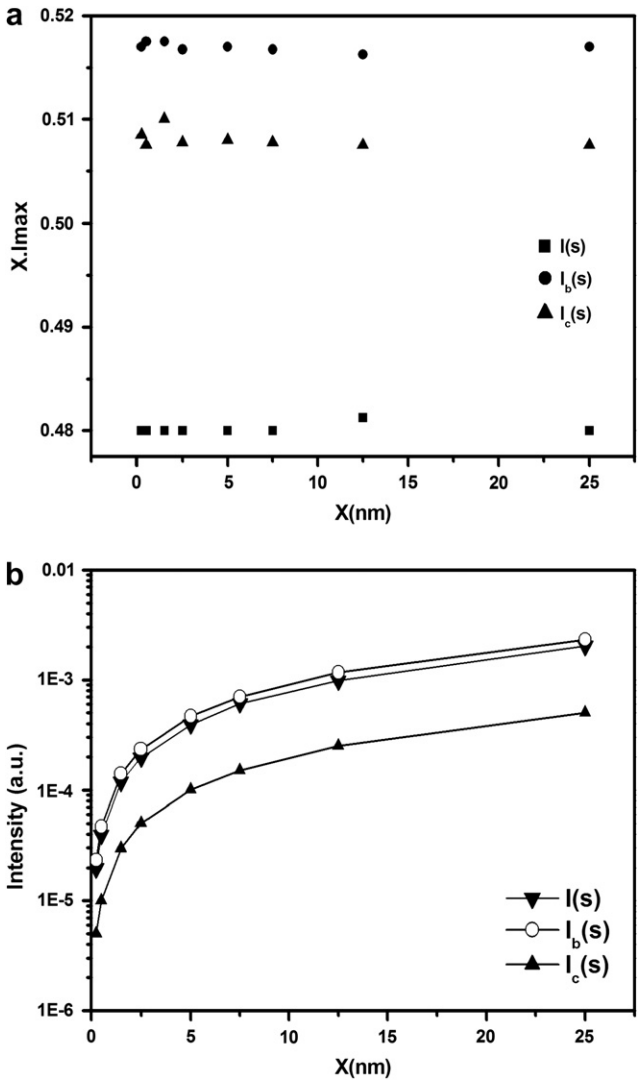

Fig. 4. (a) Typical plots of X sensitivity for mixed thickness distribution. (b) A linear relationship between X and intensity value at peak maximum for Babinet, crystalline and total intensity.

4. Results and discussions

One-dimensional SAXS pattern for neat organoclay along with different nanocomposites is shown in Fig. 6(a)–(c). Organoclay shows a strong basal reflection at $q = 1.87\ nm^{-1}$. In addition, another prominent reflection at $q = 5\ nm^{-1}$ and a weak signal at $q = 3\ nm^{-1}$ could be seen, and are attributed to the presence of clay layers that are not significantly expanded by organic modifier treatment. These peaks corresponding to neat organoclay can be monitored to assess effectiveness of organic modification and extent of exfoliation in the nanocomposite [58]. Differences in levels of nanoclay dispersion in the nanocomposites based on three different polymers HPP, RCP and ICP could be immediately seen, as indicated by differences in intensity and peak position for the organoclay SAXS response. SAXS peaks of organoclay at higher q of $5\ nm^{-1}$ and $3\ nm^{-1}$ were considerably attenuated in all three nanocomposites, whereas the basal reflection was broadened and shifted to lower q values and further a reduction in intensity was seen. This is attributed to increased exfoliation as well as expansion of clay layers on processing. Strong basal peaks were observed for HPP-NC (Fig. 6(a)) and RCP-NC (Fig. 6(b)), whereas for ICP based nanocomposites, the compounded sample ICP-NC1 (Fig. 6(c)) showed a broad hump around the basal reflection region of clay, indicating the presence of segregated clay. However, the sample processed by masterbatch route ICP-NC2 showed a SAXS response similar to that of the neat polymer, suggesting very high levels of exfoliation.

Further assessment of peak shapes and positions from regular SAXS spectra as in Fig. 6 could be difficult, these peaks being very broad in nature. Better definition of organoclay, lamellar peaks and interplanar spacings for these samples was therefore arrived at from a desmeared and Lorentz corrected SAXS spectra, after applying the data treatments explained in Section 2. Lorentz corrected SAXS spectra Iq^2 vs. q plots in the q range of 0.056–3.5 nm^{-1} for organoclay, a typical polymer HPP and its nanocomposite HPP-NC are given in Fig. 7(a)–(c). Large changes in organoclay microstructure and lamellar morphology in the nanocomposite can be readily seen.

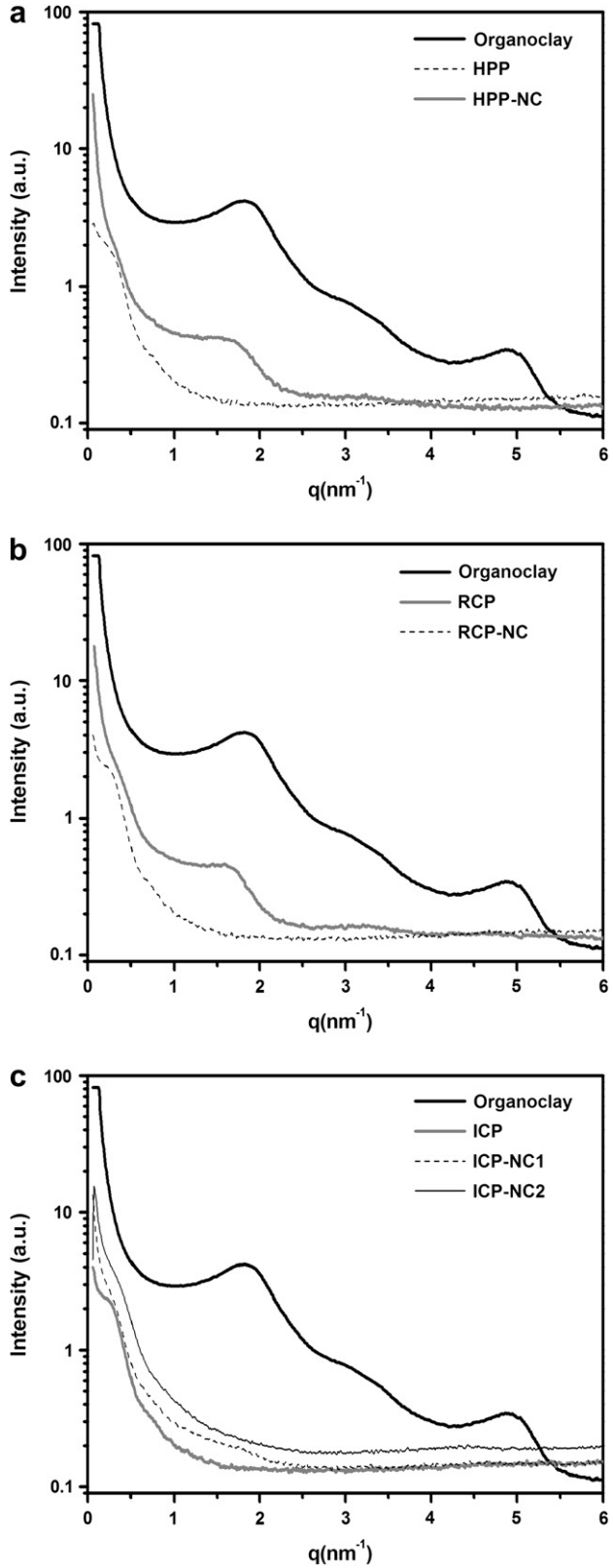

Fig. 6. X-ray scattering response for neat organoclay and the three nanocomposites. The peak at 1.8° corresponds to clay basal reflection, while the peaks at higher scattering angles represent clay layers that are not significantly expanded on organic modifier treatment.

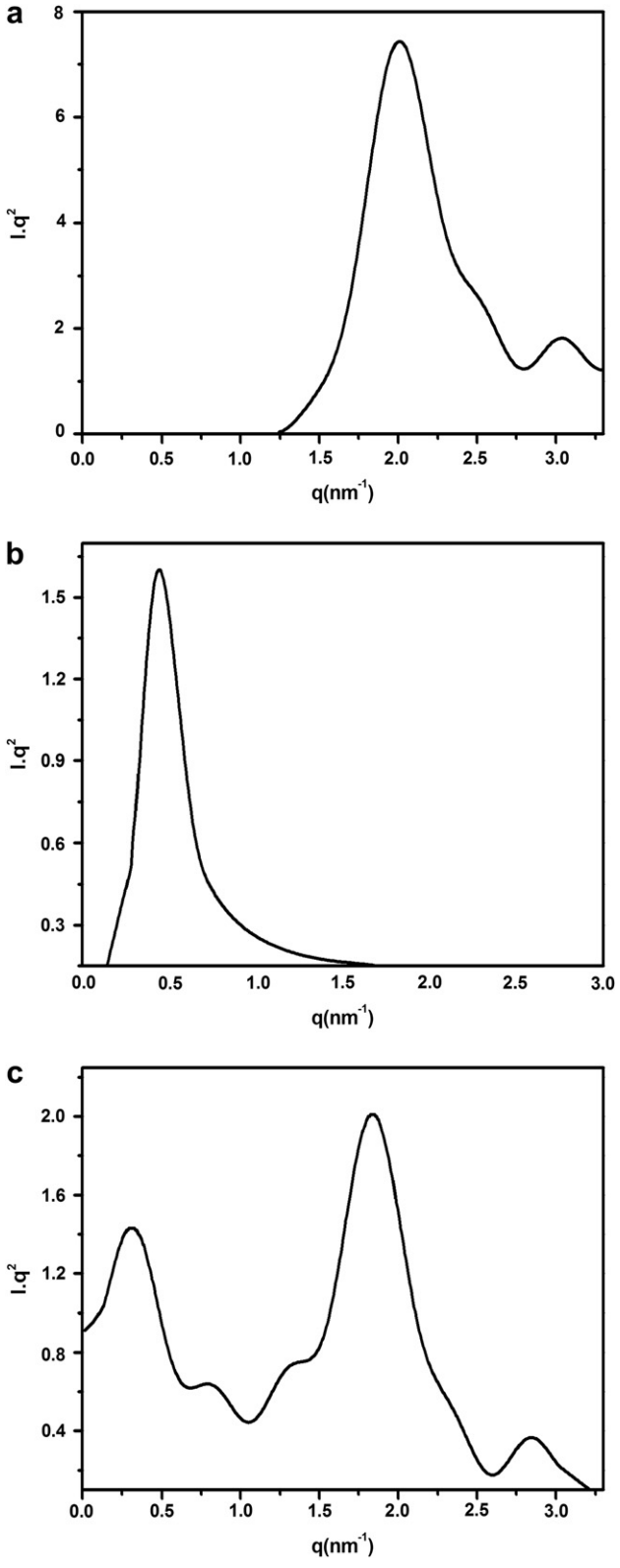

Fig. 7. Lorentz corrected SAXS spectra for HPP-NC nanocomposite and comparison to neat organoclay and neat HPP.

Differences in organoclay dispersion and resultant microstructure in nanocomposites HPP-NC, RCP-NC, ICP-NC1, ICP-NC2 relative to neat organoclay are shown in Fig. 8, in the organoclay response region. The total scattering intensity can be treated as a convolution of responses from different component populations. Extent of organoclay exfoliation, presence of component populations of organoclay with different interlayer spacing, as well as their relative fractions could be inferred for samples shown in Fig. 8. For neat

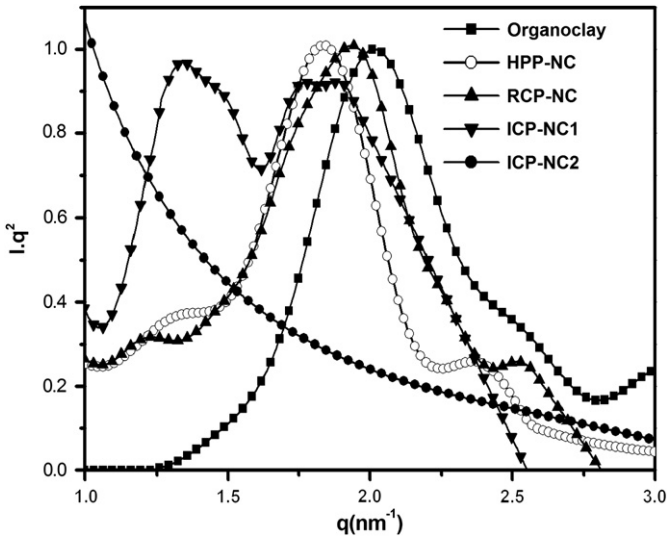

Fig. 8. Lorentz corrected SAXS spectra for PP nanocomposites and comparison to neat nanoclay. Presence of different populations corresponding to the basal nanoclay, collapsed and expanded clay layers in these samples can be clearly seen.

organoclay, three distinct peaks were seen at 2 nm^{-1}, 2.56 nm^{-1} and 3.05 nm^{-1}. Poor organoclay dispersion for HPP-NC and RCP-NC could be clearly understood, from the presence of prominent peaks corresponding to basal organoclay peak. For ICP-NC1, a very broad scattering even though of low intensity, could be identified in the Lorentz corrected spectrum. This points to less than complete exfoliation of clay tactoids in this nanocomposite, though relatively higher level of organoclay dispersion is achievable in ICP matrix compared to HPP and RCP. In the case of all three nanocomposites HPP-NC, RCP-NC and ICP-NC1, shift of organoclay basal peak position to lower scattering angle was seen in the Lorentz corrected spectra, explaining the expansion of basal clay layers. HPP-NC and RCP-NC showed a shoulder at higher scattering vector of 2.3 nm^{-1} and 2.5 nm^{-1}, respectively, attributed to unexpanded layers in neat organoclay [58]. In addition, HPP-NC and RCP-NC showed a shoulder at lower scattering angles less than $q = 1.4\ nm^{-1}$, representing a third population consisting of intercalated clay tactoids [53]. Interestingly, Lorentz corrected curves of ICP-NC2 did not show any signal from nanoclay tactoids, and could be considered truly indicative of complete exfoliation of nanoclay in this particular ICP based nanocomposite.

Detailed analysis of these SAXS spectra shown in Fig. 8 was carried out with Hosemann's model, so as to estimate quantitative morphological data. Based on SAXS response of organoclay and nanocomposites, and their component populations, model fit was carried out. As explained in Section 2, Gaussian distributions are usually used for these deconvolutions, however, allowing flexibility between symmetry and asymmetry, in this work, mixed thickness distribution was considered for deconvolution of SAXS responses, wherever applicable. Comprehensive morphological data for these samples are discussed below.

Fig. 9(a)–(f) shows model fitted SAXS spectra for neat organoclay and those for the nanocomposites HPP-NC, RCP-NC, and ICP-NC1. For neat organoclay (Fig. 9(a)), 90% of the experimental data was seen to fall under the population corresponding to basal peak, 6% of clay layers fell under an unexpanded tactoids' population, and

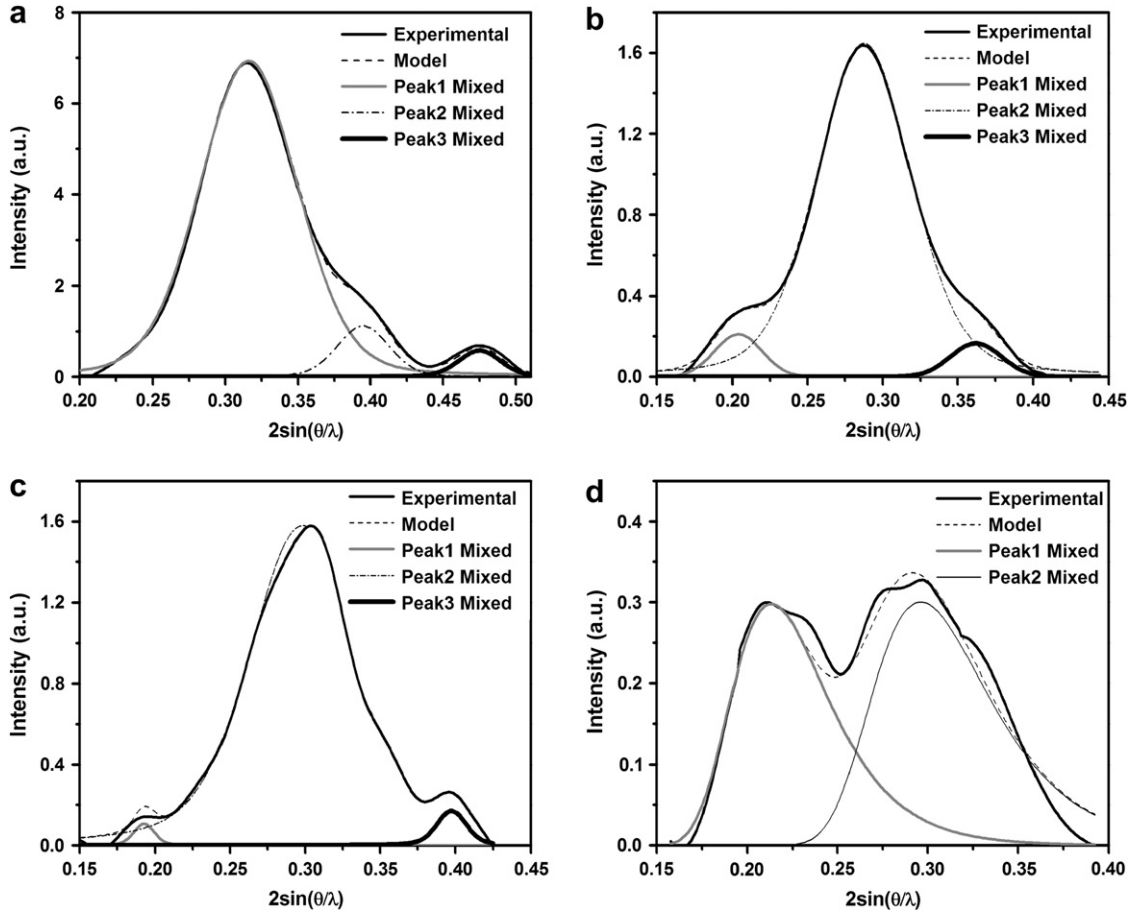

Fig. 9. Experimental and model SAXS spectra for (a) organoclay, (b) HPP-NC, (c) RCP-NC and (d) ICP-NC1.

another 4% under a second unexpanded population. Three populations were also seen for HPP-NC (Fig. 9(b)), with basal, intercalated and unexpanded populations of 89%, 6% and 5%, respectively. RCP-NC showed three populations as well (Fig. 9(c)), the highly asymmetrical SAXS data deconvoluted to a main population of 95% consisting of clay tactoids, 2% with intercalated layers and a 3% fraction of unexpanded layers. The broad SAXS response for ICP-NC1 (Fig. 9(d)) could be modeled as an intercalated single population. It may be noted that better model fit was found to be difficult for this sample as a result of high noise in the low intensity SAXS data. SAXS response for ICP-NC2 (Fig. 8) tends to the theoretical response in the *N*-sensitivity plot given in Fig. 3 fitting a completely exfoliated case.

A comparison of the structural parameters estimated from the mixed thickness distribution model for organoclay and nanocomposites is given in Table 1. Clay platelet thickness was estimated to be 1.2 nm and matched with the value supplied by the vendor for this organoclay system, and was kept constant throughout this work. Clay platelet thickness is slightly higher than the commonly reported value of about 1 nm. However, this value can be significantly influenced by the origin of the clay and processing steps involved in the organic modification. In the model used here, an ideal two-phase model is applied, and transition layer thicknesses are ignored. The calculated value of 1.2 nm from SAXS could include a contribution from this transition layer.

Differences in levels of exfoliation of nanoclay in different PP matrices could be easily understood as prominent differences in the number of clay tactoids *N* and long period *X*. *N* was seen to be >60 for the basal peak of organoclay, and was seen to reduce to 30 for HPP-NC, followed by RCP-NC with $N = 13$. High level of exfoliation, evident from the broad SAXS response for ICP-NC1 agreed well with low value of $N = 3$, whereas absence of any SAXS peaks for ICP-NC2 confirmed full exfoliation, i.e., $N = 1$. Long period $X = 3.2$ nm for neat organoclay was seen to increase from 3.2 nm to 3.5 nm, 3.3 nm and 3.6 nm for HPP-NC, RCP-NC and ICP-NC1, respectively. Differences in *N* and *X* were also seen for the peaks corresponding to smaller populations of intercalated layers and unexpanded layers in organoclay for HPP-NC and RCP-NC and are summarized in Table 1. These structural factors thus provided a comprehensive picture of morphological changes of organoclay in the nanocomposites depending on polymer matrix and processing routes.

Comparison of SAXS analysis to TEM results provided good agreement. TEM micrographs for the four nanocomposites are given in Fig. 10(a)–(d). Large agglomerates of organoclay can be readily seen in the HPP and RCP based nanocomposites while high levels of exfoliation were seen in the ICP based nanocomposites. From TEM images, it is difficult to comment on average number of layers within large aggregates, as seen in HPP-NC and RCP-NC, since the morphology will depend on regions where the TEM sections were taken from. Nevertheless, it can be clearly seen that the order of the number of layers agrees with that estimated from SAXS analysis. ICP-NC1 shows smaller clay aggregates with 2–4 layers, while ICP-NC2 showed the highest level of exfoliation, with organoclay layers dispersed mostly as individual platelets in the matrix polymer phase.

The structural parameters obtained above from Hosemann's model correlated very well with mechanical properties of the nanocomposites, especially impact and flexural modulus. For HPP-NC and RCP-NC, impact performance was seen to deteriorate upon incorporation of nanoclay, for HPP-NC the value dropped from 37 J/m^2 to 33 J/m^2, while modulus increased from 1236 MPa to 1929 MPa. Similar behavior was also found in the case of RCP-NC with a drop in impact from 493 J/m to 440 J/m while flexural modulus increased from 800 MPa to 950 MPa. Conversely, mechanical properties for ICP-NC1 showed a dramatic improvement, the impact value for this sample increased from 165 J/m^2 to 198 J/m^2 and flexural modulus increased from 1000 MPa to 1440 MPa. ICP-NC2 exhibited even further increase in impact from 165 J/m for neat ICP to 230 J/m for the nanocomposite. Flexural modulus also increased from 1000 MPa to 1563 MPa. A plot of percentage change in impact for the three nanocomposites was made as a function of number of clay layers *N* for the major population, i.e., the basal peak, as given in Fig. 11. Though dependence of physical properties on number of clay layers and existence of different organoclay populations in the nanocomposites have been reported [50,51,53], above plot provides a direct correlation of *N* as a key structural parameter translating to material performance. With decrease in *N*, percentage change shift from negative to positive axis could be seen, with $N = 1$ resulting in improvement of impact by 40%. Thus, *N*, together with *X*, can be used as a powerful parameter to monitor nanoclay exfoliation/dispersion and optimize material and processing parameters for the preparation of nanocomposites. Estimation of level of exfoliation has also been demonstrated using an integrated correlation functions' approach, with a new parameter introduced as exfoliation factor as a measure of extent of exfoliation, and will be communicated in a future correspondence [59].

It may be noted that addition of nanoclay leads to breakup and better dispersion of discrete EPR particles, and hence the impact performance for such a three-phase system is an interplay between EPR morphology and nanoclay dispersion [54,60]. Since ICP is a three component system with dispersed organoclay and EPR phases in PP matrix, possible changes in EPR morphology were explored to understand further factors leading to improved impact performance of ICP-NC1, in addition to high level of organoclay exfoliation, as explained earlier. Improvement in impact properties with improved exfoliation has been described to be due to the arresting of crack path by exfoliated clay layers [61]. In addition, refinement of EPR particle size to an optimum value could be understood from the TEM micrographs for neat ICP and ICP-NC1

Table 1
Structural parameters for nanoclay estimated from Hosemann's model application to SAXS response employing mixed thickness distribution

Sample	Population	% Population	*X*	*H*	*L*	*N*	σ_H	σ_L	σ_{HG}	σ_{HE}	σ_{LG}	σ_{LE}
Organoclay	Basal	90	3.3	1.2	2.1	>60	0.27	0.38	0.10	0.10	0.40	0.60
	Unexpanded 1	6	2.5	1.2	1.3	>60	0.44	0.52	0.15	0.20	0.20	0.20
	Unexpanded 2	4	2.2	1.2	1	>60	0.47	0.42	0.15	0.12	0.10	0.12
HPP-NC	Basal	89	3.5	1.2	2.3	30	0.27	0.76	0.10	0.50	0.30	0.40
	Intercalated	6	4.9	1.2	3.7	15	0.42	1.25	0.20	0.60	0.20	0.60
	Unexpanded	5	2.7	1.2	1.5	35	0.46	0.55	0.17	0.20	0.15	0.20
RCP-NC	Basal	95	3.3	1.2	2.1	15	0.35	0.61	0.20	0.40	0.30	0.40
	Intercalated	2	5.2	1.2	4	18	0.40	1.42	0.15	0.60	0.20	0.60
	Unexpanded	3	2.5	1.2	1.3	32	0.48	0.49	0.12	0.10	0.12	0.15
ICP-NC1	Basal	100	3.6	1.2	2.4	3	0.27	0.55	0.30	0.60	0.31	0.65
ICP-NC2	–	–	1.2	–	1	–	–	–	–	–	–	–

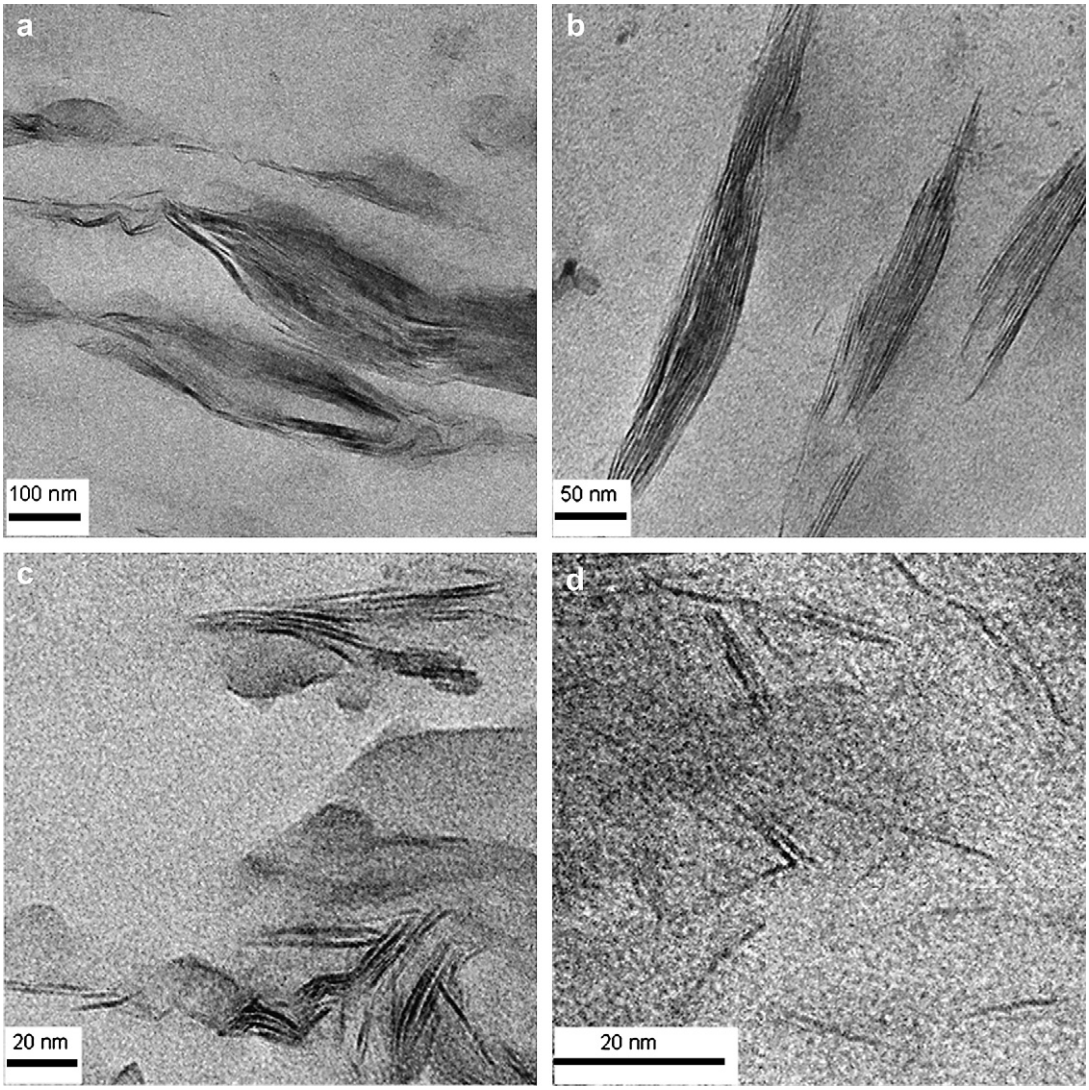

Fig. 10. TEM micrographs showing organoclay dispersion in different PP matrix phases: (a) HPP-NC, (b) RCP-NC, (c) ICP-NC1 and (d) ICP-NC2.

(Fig. 12(a)–(c)). EPR particle size changed from a mean size of 3–4 μm for ICP to 1.5 μm for ICP-NC1, agreeing with the reported trend [60]. Better dispersion of EPR was also observed in the nanocomposite, while EPR particles were seen as agglomerates with irregular size and shape in ICP. Nanoclay particles were seen to lie primarily in PP matrix phase. TEM micrograph of EPR rubber recorded at higher magnification (Fig. 12(c)) did not show any features indicative of crystalline phases inside EPR rubber phase that could lead to drastic drop in efficiency of EPR as an impact modifier. Thus, EPR morphology in ICP-NC1 was found to be ideal in enabling its performance as a nanocomposite, when combined with good dispersion of nanoclay, resulting in superior mechanical properties.

Changes in the crystallographic organizations of PP, typically induced by incorporation of nanomaterials were also investigated by wide angle X-ray scattering (WAXS). Fig. 13(a)–(c) shows WAXS spectra in the 2θ range 10°–24° for HPP, RCP and ICP samples and their respective nanocomposites. In all samples, peaks corresponding mainly to α polytype of PP could be identified. For the neat PP samples, peaks observed at 2θ values of 14.1°, 16.9°, 18.6°, 21.6° and 21.9° correspond to (110), (040), (130), (111) and (041) planes of the α phase of PP. An additional peak at $2\theta = 20.1°$, corresponding to γ(117) was noted in RCP [62]. An increase in peak

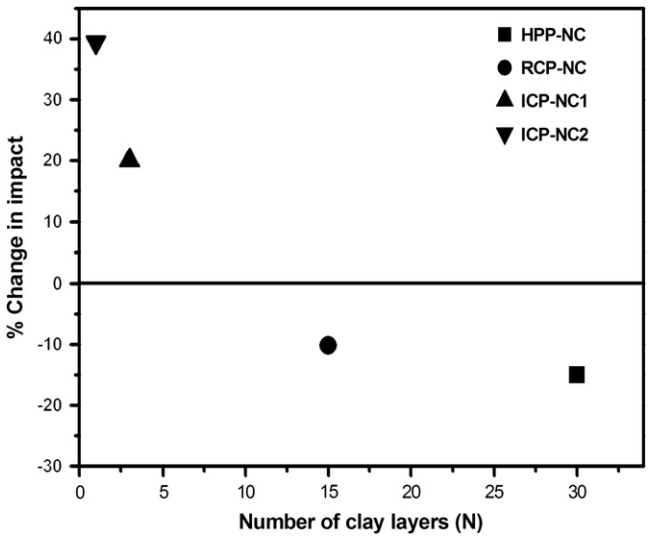

Fig. 11. Plot of percentage variation in impact for the nanocomposites as a function of number of clay layers.

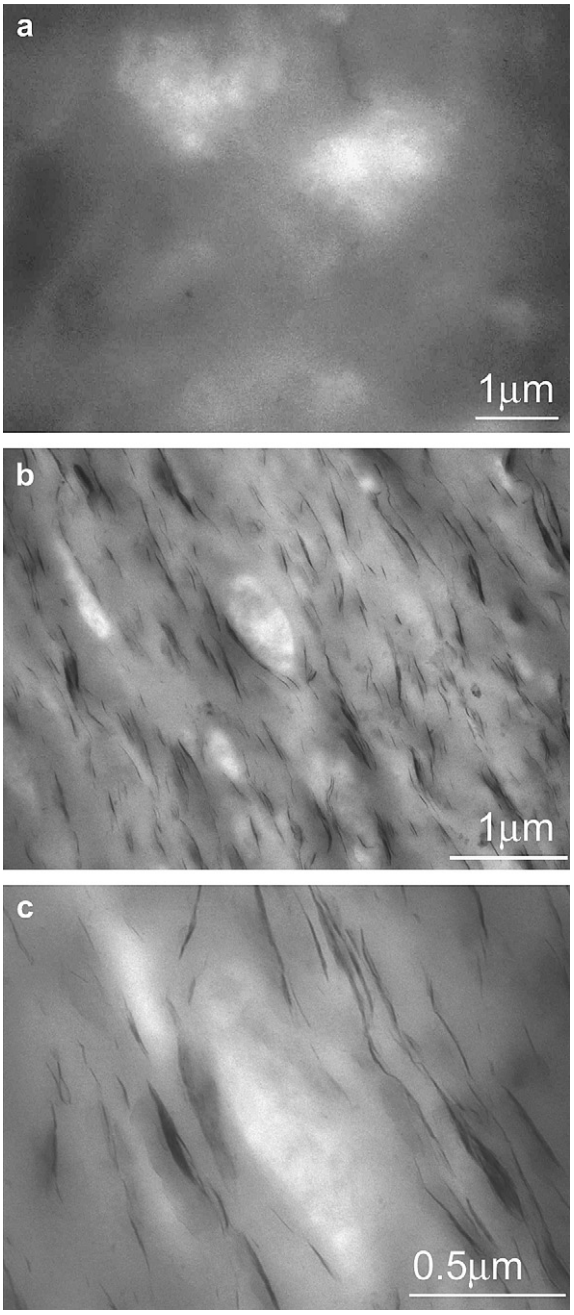

Fig. 12. TEM micrographs for (a) ICP and (b) ICP-NC1 showing the mechanism of improved impact properties in the nanocomposite. Better dispersion of EPR can be seen in ICP-NC1. (c) EPR rubber morphology at higher magnification does not show any evidence of crystallization within EPR phase.

intensity for γ(117) was seen in all nanocomposites. While HPP-NC showed only marginal increase, prominent increase was seen in RCP-NC, ICP-NC1 and ICP-NC2. Origin of γ polytype of PP is thought to be caused by incorporation of defects, even at very small concentrations, in the long isotactic sequences of PP [62]. γ-Form of PP is usually obtained under particular conditions such as elevated pressures [63] or from iPP with low molecular weight [64]. Increased γ-fraction in PP has also been reported in the presence of organoclay [54,65,66], pointing to the role of organoclay in promoting γ-fraction of PP. This effect has been ascribed to decreased chain mobility induced by clay particles, leading to the formation of smaller, less ordered crystallites [65]. In RCP and ICP, the γ-fraction is also introduced by ethylene co-monomer [49] and

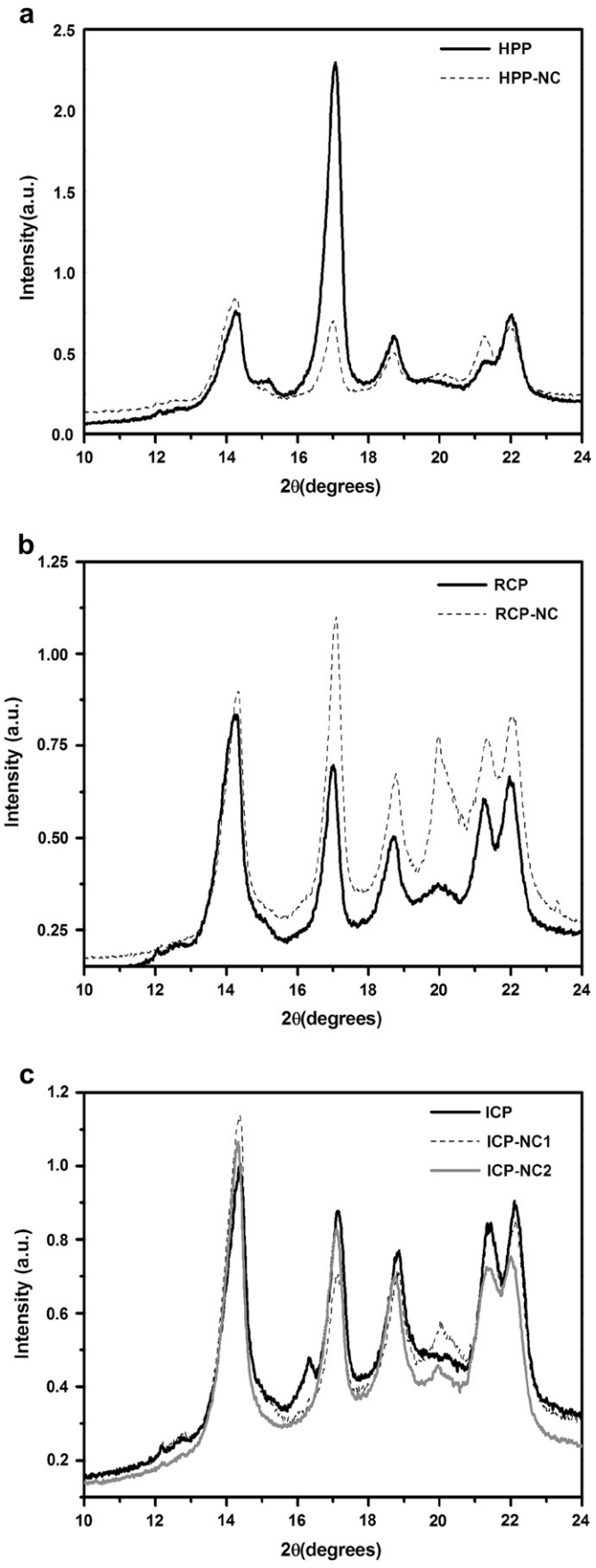

Fig. 13. WAXS spectra for PP nanocomposites and comparison to that of PP matrix. (a) HPP and HPP-NC, (b) RCP and RCP-NC and (c) ICP, ICP-NC1 and ICP-NC2. Increased intensity for γ(117) peak can be seen for all the three cases.

Table 2
Bulk crystallinity and percentage γ/α estimated for three PP matrices, i.e., HPP, RCP and ICP and their nanocomposites

Sample	Φ (WAXS)	Φ (SAXS)	% γ(WAXS)	% γ(SAXS)
HPP	68	87	–	–
HPP-NC	57	75	–	–
RCP	58	71	10	6
RCP-NC	62	68	53	69
ICP	54	70	–	–
ICP-NC1	52	74	13	7
ICP-NC2	52	74	12	8

additionally by nanosized filler in the nanocomposites. For the three polymers and their nanocomposites, relative content of γ form with respect to α form was estimated from WAXS and is shown in Table 2. Since the wide angle X-ray diffraction profiles for α and γ forms of PP are very similar, ratio of intensity of $\gamma(117)$ peak to that of a distinct $\alpha(130)$ peak was taken as a measure of γ fractions in the polymer [62]. Percentage γ/α could not be estimated for HPP and HPP-NC, the signal intensity being very low. For RCP, RCP-NC, ICP-NC1 and ICP-NC2, percentage γ/α was found to be 10, 53, 13 and 12, respectively. It may be noted that RCP showed a very high increase in γ from an initial value of 16% to 53% in RCP-NC. Overall, efficiency of nanoclay in improving γ nucleation in all three types of PP was seen, with varying degrees in different types of polypropylene. Efficiency of nanoclay as nucleator for polypropylene has been reported with nanoclays of different origin and organic modifier treatment [67]. Total crystallinity estimated from WAXS spectra for PP samples and their respective nanocomposites are also given in Table 2. Introduction of nanoclay resulted in change of total crystallinity for all the three samples. While a decreasing trend in total crystallinity was seen for HPP, comparable bulk crystallinity was observed for RCP and ICP.

Changes in crystallographic structures of PP with nanoclay incorporation in PP nanocomposites also resulted in large changes in its lamellar structures, as expected. SAXS spectra plotted in the lamellar region for neat PP and its corresponding nanocomposites are shown in Fig. 14(a)–(c). For HPP, a main peak at $q = 0.38\ \mathrm{nm}^{-1}$ was seen. For the nanocomposites HPP-NC, shift in the peak position to lower angles followed by peak broadening was seen. In RCP and RCP-NC, SAXS response was seen to consist of two prominent peaks, and is attributed to the presence of α and γ lamellae. Lamellar thickness for γ crystals is usually lower, so the peak at higher q is assigned to γ lamellae in both the samples [54]. SAXS peaks corresponding to both α and γ lamellae in RCP showed a significant shift to lower angles in RCP-NC. ICP based nanocomposites ICP-NC1 as well as ICP-NC2 also showed appearance of γ peaks at smaller concentrations. Peak position for α lamellae in ICP-NC1 was not considerably shifted while ICP-NC2 showed a small shift to higher q, indicating lessening of lamellar thickness. Percentage γ/α in the nanocomposites could now be easily estimated from peak areas in SAXS spectra and was found to be 12, 65, 10 and 14 for RCP, RCP-NC, ICP-NC1 and ICP-NC2, respectively. Thus, SAXS method also provides an accurate method to estimate local γ/α in the lamellar region, and agreed with the trend seen in WAXS.

Hosemann's models were also applied to the lamellar SAXS response region of HPP, RCP, ICP and their nanocomposites, in order to understand changes in the lamellar morphology of PP upon nanoclay incorporation. Mixed thickness distribution was used to derive detailed structural parameters for α and γ populations for these samples and is summarized in Table 3. Notable changes were observed in N and X, in general, N showed a decrease in the nanocomposites for both α and γ lamellae. HPP and RCP showed considerable increase in long period, with reference to neat polymer. Long period for ICP-NC1 was comparable to ICP, while ICP-NC2 showed lower value for long period. Differences in lamellar

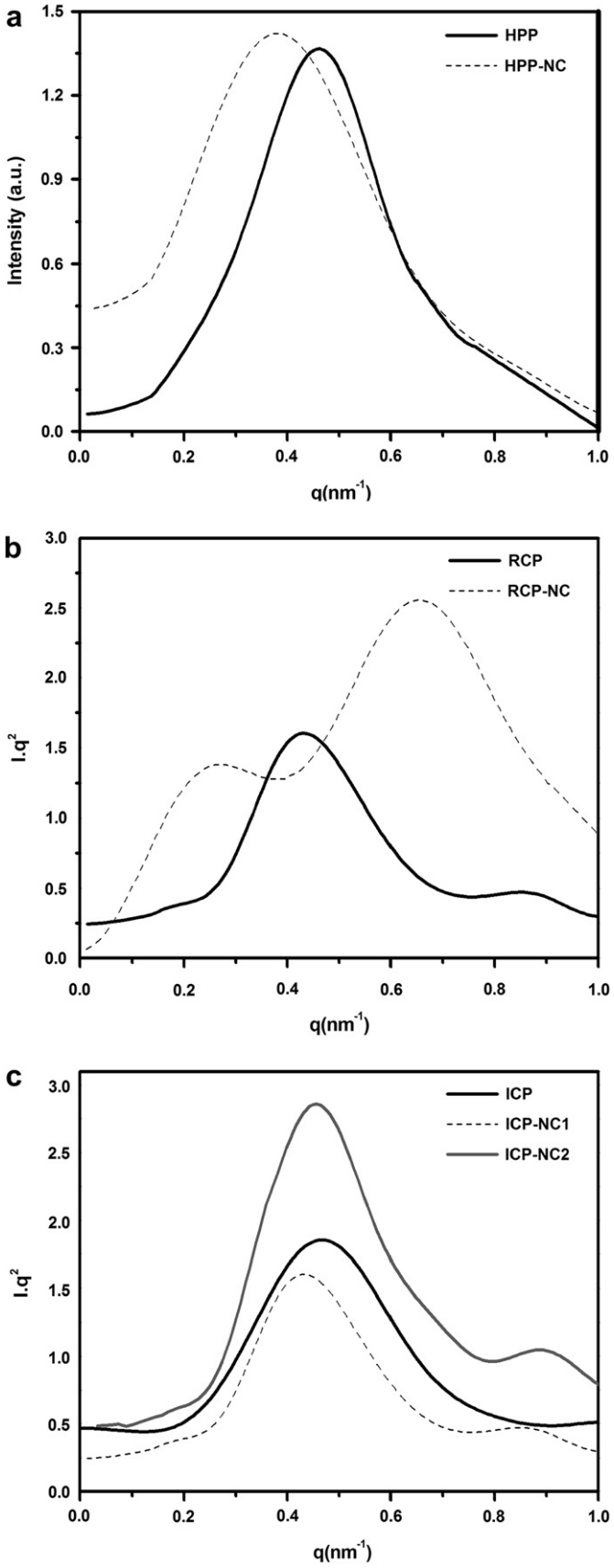

Fig. 14. Typical SAXS spectra in the lamellar region for HPP and its nanocomposite. The peak at lower scattering angle corresponds to α lamellae, which is shifted to lower scattering vector in nanocomposites. The peak at higher scattering angle represents γ lamellae and is prominent in RCP-NC.

Table 3
Lamellar structural parameters estimated from SAXS response for α and γ population of neat polymers and nanocomposites

Sample	Lamellae	% Population	*X*	*H*	*L*	*N*	σ_H	σ_L	σ_{HG}	σ_{HE}	σ_{LG}	σ_{LE}
HPP	α	100	14.0	12.2	1.8	25	3.1	0.4	3.0	0.4	3.0	0.5
HPP-NC	α	100	16.0	12.1	3.9	20	2.1	0.9	4.0	1.5	4.0	1.0
RCP	α	94	14.0	10.0	4.0	15	2.0	0.8	3.0	1.2	3.0	1.2
	γ	6	7.4	5.4	2.0	12	2.0	0.7	0.7	0.2	0.7	0.3
RCP-NC	α	31	24.0	17.3	6.7	5	2.7	0.3	5.6	1.0	6.0	3.0
	γ	69	9.0	6.0	3.0	7	2.5	1.2	2.0	1.0	0.5	0.3
ICP	α	100	14.0	10.6	3.4	13	1.4	0.6	2.2	1.0	2.5	1.0
ICP-NC1	α	93	14.0	10.5	3.5	15	2.3	0.8	3.1	1.1	3.0	0.9
	γ	7	7.4	4.9	2.5	12	1.5	0.7	1.0	0.5	1.0	0.5
ICP-NC2	α	92	12.8	8.8	4.0	11	1.4	0.6	3.0	1.3	3.0	1.4
	γ	8	7.2	5.0	2.2	12	1.5	0.6	1.2	0.5	1.0	0.5

thicknesses in the nanocomposites are related to multiple parameters such as initial crystal structure of PP matrix, nucleators and dispersed phases, processing conditions, etc., hence further investigations would be required to comprehensively explain the changes seen in lamellar thickness of nanocomposites. Changes in α lamellar thicknesses reported on a PP-EPR composition [54] were found to lie in the range of 15.8–17.4 nm for the nanocomposites as compared to 16.7 nm for neat PP-EPR. Local crystallinity Φ was also estimated as a weighted average of H/L for the γ fraction and α fraction and is given in Table 2. Comparable trend in Φ was seen for the three polymers as estimated from WAXS, but it should be noted that SAXS estimates local crystallinity from the lamellar stacks, while WAXS data provide bulk crystallinity in the samples.

5. Conclusions

Dispersion of organoclay in different types of PP matrices and changes in lamellar morphology as a result of organoclay incorporation were studied by small angle X-ray scattering. One-dimensional models conventionally applied to study lamellar stacks of semicrystalline polymers were extended to the study of similarly ordered organoclay structures. A mixed thickness distribution was applied on Lorentz corrected SAXS spectra and quantitative data related to organoclay dispersion were achieved, key parameters being the number of tactoids *N* and long period *X*. Differences in organoclay dispersion in HPP, RCP and ICP could be explained in detail and related well with mechanical properties. In neat organoclay, three different populations were identified: a primary population consisting of organically modified basal layers with long period of 3.3 nm, and two small populations of unexpanded layers with long period 2.5 nm and 2.2 nm. In the HPP and RCP based nanocomposites, consistent expansion of these layers was observed, in addition to the presence of a population with intercalated clay platelets. High level of organoclay dispersion could be achieved in ICP based nanocomposite, where a broad diffraction peak represents a population with a long period of 3.6 nm. *N* was observed to be 3 for PP-EPR, compared to 30 and 15, respectively, for the primary populations in HPP and RCP, as compared to a very high value of >60 for neat organoclay. Mechanism of improvement of physical properties for ICP was understood from TEM analysis as breakup and better dispersion of EPR domains along with good nanoclay dispersion. Further exfoliation of organoclays and consequently further improvement in mechanical properties for ICP could be achieved by employing a masterbatch approach, resulting in complete exfoliation of organoclay, i.e., $N = 1$.

Changes in crystal structure and percentage crystallinity in PP induced by addition of organoclay were studied by WAXS. For all three types of PP studied, growth of γ polytype of PP was seen; and was higher for RCP. Changes in lamellar structures in the nanocomposites also confirmed polymorphism in PP, on addition of nanoclay. Structural parameters for α and γ lamellae were obtained with application of the mixed thickness distribution.

Acknowledgement

Authors are thankful to the Central Facility of IIT Bombay and the Department of Chemical Engineering and Material Science, University of Minnesota, Minneapolis, MN 55455, USA for high resolution TEM images during JRB's stay as Piercy Distinguished Visiting Professor. Parts of this work were carried out in the Institute of Technology Characterization Facility, University of Minnesota, which receives partial support from NSF through the NNIN program. Microscopy assistance of Shobha Ramagiri and M A Arunagirinathan is gratefully acknowledged.

References

[1] Hussain F, Hojjati M, Okamoto M, Gorga RE. J Compos Mater 2006;40:1511.
[2] LeBaron PC, Wang Z, Pinnavaia TJ. Appl Clay Sci 1999;15:11.
[3] Ray SS, Okamoto M. Prog Polym Sci 2003;28:1539.
[4] Giannelis EP. Adv Mater 1996;8:29.
[5] Okamoto M. In: Nalwa HS, editor. Encyclopedia of nanoscience and nanotechnology, vol. 8. Stevenson Ranch, CA: American Scientific Publishers; 2004. p. 1.
[6] Vaia RA, Giannelis EP. MRS Bull 2001;26:394.
[7] Kojima Y, Usuki A, Kawasumi M, Fukushima Y, Okada A, Kurauchi T, et al. J Mater Res 1993;8:1179.
[8] Fischer H. Mater Sci Eng C 2003;23:763.
[9] Messersmith PB, Giannelis EP. J Polym Sci Part A Polym Chem 1995;33:1047.
[10] Vaia RA, Price G, Ruth PN, Nguyen HT, Litchenhan J. Appl Clay Sci 1999;15:67.
[11] Okada A, Kawasumi M, Usuki A, Kojima Y, Kurauchi T, Kamigaito O. MRS Symp Proc 1990;171:45.
[12] Alexandre M, Dubois P. Mater Sci Eng 2000;28:1.
[13] Ding Y, Guo C, Dong J, Wang Z. J Appl Polym Sci 2006;102:4314.
[14] Vaia RA, Ishii H, Giannelis EP. Chem Mater 1993;5:1694.
[15] Hasegawa N, Okamoto H, Kato M, Usuki A, Sato N. Polymer 2003;44:2933.
[16] Bergman JS, Chen H, Giannelis EP, Thomas MG, Coates GW. Chem Commun 1999:2179.
[17] Lee EC, Meilewski DF, Baird RJ. Polym Eng Sci 2004;44:1773.
[18] Usuki A, Kato M, Okada A, Kurauchi T. J Appl Polym Sci 1997;63:137.
[19] Galli P, Vecellio G. J Polym Sci Part A Polym Chem 2003;42:396.
[20] Kawasumi M, Hasegawa N, Kato M, Usuki A, Okada A. Macromolecules 1997;30:6333.
[21] García-López D, Picazo O, Merino JC, Pastor JM. Eur Polym J 2003;39:945.
[22] Lertwimolnun W, Vergnes B. Polymer 2005;46:3462.
[23] Sun T, Garces JM. Adv Mater 2002;14:128.
[24] Manke CW, Gulari E, Mielewski DF, Lee EC. US Patent, 6469073B1; 2002.
[25] Morgan AB, Gilman JW. J Appl Polym Sci 2003;87:1329.
[26] Kanny K, Moodley VK. J Eng Mater Technol 2007;129:105.
[27] Huang X, Lewis S, Brittain WJ, Vaia RA. Macromolecules 2000;33:2000.
[28] Koo CM, Kim SO, Chung JJ. Macromolecules 2003;36:2748.
[29] Lincoln DM, Vaia RA, Wang Z-G, Hsiao BS. Polymer 2001;42:1621.
[30] Vaia RA, Jandt KA, Krammer EJ, Giannelis EP. Chem Mater 1996;8:2628.
[31] Bafna A, Beaucage G, Mirabella F, Mehta S. Polymer 2003;44:1003.
[32] VanderHart DL, Asano A, Gilman JW. Macromolecules 2001;34:3819.
[33] Loo LS, Gleason KK. Polymer 2004;45:5933.
[34] Nascimento GM, Constantino VRL. Macromolecules 2002;35:1419.
[35] Vonk CG, Kortleve G. Kolloid Z Z Polym 1967;220:19.
[36] Santa Cruz C, Stribeck N, Zachmann HG, Baltá Calleja FJ. Macromolecules 1991;24:5980.
[37] Goderis B, Reynaers H, Koch MHJ, Mathot VBF. J Polym Sci Part B Polym Phys 1999;37:1715.
[38] Tonelli C, Ajroldi G, Marigo A, Marega C, Turturro A. Polymer 2001;42:9705.
[39] Verma R, Marand H, Hsiao B. Macromolecules 1996;29:7767.
[40] Hosemann R, Bagchi SN. Direct analysis of diffraction by matter. Amsterdam: North Holland; 1962.
[41] Blundell DJ. Polymer 1978;19:1258.
[42] Ruland W. Colloid Polym Sci 1977;255:417.
[43] Wang Z-G, Hsiao BS, Fu BX, Liu L, Yeh F, Sauer BB, et al. Polymer 2000;41:1791.
[44] Samon JM, Schultz JM, Hsiao BS, Khot S, Johnson HR. Polymer 2001;42:1547.
[45] Zhu P, Edward G. Polymer 2004;45:2603.
[46] Zhu P, Tung J, Edward G. Polymer 2005;46:10960.
[47] Vleeshouwers S. Polymer 1997;38:3213.
[48] Marega C, Marigo A, Cingano G, Zannetti R, Paganetto G. Polymer 1996;37:5549.
[49] Marigo A, Causin V, Marega C, Ferrari P. Polym Int 2004;53:2001.
[50] Bennetti EM, Causin V, Marega C, Marigo A, Ferrara G, Ferraro A, et al. Polymer 2005;46:8275.
[51] Causin V, Marega C, Marigo A, Ferrara G, Idiyatullina G, Fantinel F. Polymer 2006;47:4773.

[52] Ruland W, Smarsly B. J Appl Crystallogr 2004;37:575.
[53] Causin V, Marega C, Marigo A, Ferrara G. Polymer 2005;46:9533.
[54] Causin V, Marega C, Marigo A, Ferrara G, Ferraro A, Selleri R. J Nanosci Nanotechnol 2008;8:1823.
[55] Glatter O. J Appl Crystallogr 1977;10:415.
[56] Kortleve G, Vonk CG. Kolloid Z Z Polym 1968;225:124.
[57] Tsvankin DY. Polym Sci USSR 1964;6:2358.
[58] Kato M, Matsushita M, Fukumori K. Polym Eng Sci 2004;44:1205.
[59] Rasheed ASA, Preschilla N, Sivalingam G, Tyagi S, Biswas A, Bellare J. Polymer, in preparation.
[60] Mehta S, Mirabella FM, Rufener K, Bafna A. J Appl Polym Sci 2004;92:928.
[61] Modesti M, Lorenzetti D, Bon D, Beco S. Polymer 2005;46:10237.
[62] Auriemma F, De Rosa C. Macromolecules 2002;35:9057.
[63] Kojima M. J Polym Sci Part A-2 1968;6:1255.
[64] Thomann R, Semke H, Maier RD, Thomann Y, Scherrble J, Mulhaupt R, et al. Polymer 2001;42:4597.
[65] Nam PH, Maiti P, Okamoto M, Kotaka T, Hasagewa N, Usuki A. Polymer 2001;42:9633.
[66] Zheng W, Lu X, Toh CL, Zheng TH, He C. J Polym Sci Part B Polym Phys 2004;42:1810.
[67] Pozsgay A, Tünde F, László P, István S, Béla P. J Macromol Sci 2002;41:1249.